REPORT DOCUMENTATION PAGE

The public reporting burden for this collection of information is estimated to average 1 hour per response, including the time for reviewing instructions, searching existing data sources, gathering and maintaining the data needed, and completing and reviewing the collection of information. Send comments regarding this burden estimate or any other aspect of this collection of information, including suggestions for reducing the burden, to the Department of Defense, Executive Services and Communications Directorate (0704-0188). Respondents should be aware that notwithstanding any other provision of law, no person shall be subject to any penalty for failing to comply with a collection of information if it does not display a currently valid OMB control number.
PLEASE DO NOT RETURN YOUR FORM TO THE ABOVE ORGANIZATION.

1. REPORT DATE (DD-MM-YYYY)	2. REPORT TYPE	3. DATES COVERED (From - To)
01-02-2007	Final	15-07-2002 - 14-07-2006

4. TITLE AND SUBTITLE

Emissions Control in Swirl Stabilized Spray Combustors, an Experimental and Computational Study

5a. CONTRACT NUMBER

N00014-02-01-0837

5b. GRANT NUMBER

5c. PROGRAM ELEMENT NUMBER

05PR02238-01

6. AUTHOR(S)

Ephraim Gutmark

5d. PROJECT NUMBER

5e. TASK NUMBER

5f. WORK UNIT NUMBER

7. PERFORMING ORGANIZATION NAME(S) AND ADDRESS(ES)

University of Cincinnati
Office of Vice President Univ Dean for Grad Studies Research
305 Clifton Ave WM Taft Road, Cincinnati, OH 45221-0627

8. PERFORMING ORGANIZATION REPORT NUMBER

9. SPONSORING/MONITORING AGENCY NAME(S) AND ADDRESS(ES)

Stephen W. McElvany, ONR 331
Office of Naval Research
875 N. Randolph St., One Liberty Center
Arlington, VA 22203-1995

10. SPONSOR/MONITOR'S ACRONYM(S)

11. SPONSOR/MONITOR'S REPORT NUMBER(S)

12. DISTRIBUTION/AVAILABILITY STATEMENT

No limitations

13. SUPPLEMENTARY NOTES

14. ABSTRACT

Detailed measurements of velocity statistics, temperature distribution, flame chemiluminescence, and emission characteristics in a lean direct fuel injection multiswirl gas turbine combustor were acquired. The inlet and exit boundary conditions, including the mixing tube length and the exhaust nozzle contraction ratio, were modified to emphasize the effects of these boundary conditions on the characteristics of nonreacting and reacting flows. Velocity statistics, including mean and turbulence kinetics, were measured by using SPIV in a cylindrical combustor chamber for isothermal and reacting flow cases. The velocity spectra at different locations were measured using hot-wire anemometry. The temperature distribution along the combustor radial direction was measured using thermocouples at different axial locations for a variety of multi-swirl configurations. The exhaust emissions of NOx and CO were measured as a function of fuel/air ratio. The data along with the detailed description of the experimental setup and operating conditions can be used to validate modeling approaches to swirling flows, the turbulence/chemistry interaction.

15. SUBJECT TERMS

Combustion, emissions, gas turbines, swirling flow

16. SECURITY CLASSIFICATION OF:			17. LIMITATION OF ABSTRACT	18. NUMBER OF PAGES	19a. NAME OF RESPONSIBLE PERSON
a. REPORT	b. ABSTRACT	c. THIS PAGE			Ephraim Gutmark
UU	UU	UU	UU	48	19b. TELEPHONE NUMBER (Include area code) (513) 556-1227

Emissions Control in Swirl Stabilized Spray Combustors, an Experimental and Computational Study

Final Report for contract no. N00014-02-01-0837

Ephraim J. Gutmark

Department of Aerospace Engineering and Engineering Mechanics

University of Cincinnati

Cincinnati, OH 45221-0070

Tel: (513) 556-1227

E mail: Ephraim.Gutmark@uc.edu

1

Nomenclature

C_R	Contraction Ratio of Exhaust Nozzle
D	Diameter of Swirler Exit
D_c	Diameter of Combustion Chamber
f	Frequency
k	Turbulence Kinetic Energy
L_{mt}	Nondimensional Length of Mixing Tube
m_a	Mass Flow Rate of Air
r	Radial Coordinates
R	Radius of Swirler Exit
P_3	Plenum Pressure
S_{tD}	Strouhal Number
T_3	Air Inlet Temperature
T_4	Combustion Gas Temperature
V_0	Averaged Axial Velocity Based on Swirler Exit
V_r	Radial Velocity Component
V_z	Axial Velocity Component
V_θ	Tangential Velocity Component
z	Axial Coordinates
Φ	Fuel Equivalence Ratio
Φ_{LBO}	Fuel Equivalence Ratio at Lean Flame Blow Off

List of Tables

List of Figures

Abstract

Detailed measurements of velocity statistics, temperature distribution, flame chemiluminescence, and emission characteristics in a Lean Direct fuel Injection multi-swirl gas turbine combustor are presented. The inlet and exit boundary conditions, including the mixing tube length and the exhaust nozzle contraction ratio, were modified to emphasize the effects of these boundary conditions on the characteristics of non-reacting and reacting flows. Velocity statistics, including mean and turbulence kinetics, were measured using stereoscopic Particle Imaging Velocimetry in a cylindrical combustor chamber for isothermal and reacting flow cases. The velocity spectra at different locations were measured using hotwire anemometry. Temperature distribution along the combustor radii was measured using type-B fine thermocouple at different axial locations for a variety of multi-swirl configurations. The exhaust emissions of NO_x and CO were sampled for different fuel equivalence ratios. The data and the detailed description of the experimental setup and operating conditions can be used to support LES predictions of swirling flow fields and the chemistry/turbulence interaction in multi-swirl gas turbine combustors.

Introduction

Increasingly stringent regulations on pollutant emissions of gas turbine engines, particularly regarding low emissions of oxides of nitrogen (NO_x), require development of new concepts of combustion systems[1]. Typical method of reducing NO_x formation is by operating the combustor in a lean premixed combustion mode near the Lean Blow-Out Limit (LBO). This type of approach results in efficient combustion with extremely low emissions and improved combustor performance. Lean premixed combustors achieve NO_x emission levels below 10 PPM at atmospheric pressure and below 25 PPM at gas turbine operating conditions [2, 3]. Reliability of

5

lean premixed combustion systems is challenging as they operate close to the lean stability limit and are more susceptible to combustion instabilities, flame blowout and flashback[4].

As an alternative approach, Lean Direct fuel Injection (LDI) combustion, one of the new concepts that are applied in non-premixed combustion, is developed to reduce NO_x emissions through the arrangement of multiple counter-rotating or co-rotating air swirlers with a distributed fuel injection system[5,6]. Such an arrangement allows control of the mixing pattern, flame structure, and temperature via air flow control and fuel distribution to prevent drawbacks associated with premixing flames, such as auto-ignition and flashback[7,8]. Experimental study[8] showed that the NO_x emissions for a LDI type double-swirler burner were less than half of the conventional small-hub and large-hub swirlers. LDI combustors are advantageous in providing low NO_x emissions with lower susceptibility to combustion dynamics and thus provide an attractive alternative for application in aircraft gas turbine engines. Triple Annular Research Swirler, which has been developed through collaboration with GE Aircraft Engines and Goodrich Aerospace, features the generic design of LDI fuel injectors with three individual air swirlers coupled with two separate fuel supply lines for liquid fuel. This nozzle/swirler assembly can also be configured for use with gaseous fuels.

Large Eddy Simulation (LES), which is a CFD technique bridging between Direct Numerical Simulation (DNS) and Reynolds Averaged Navier-Stokes (RANS) simulation, provides cost-effective solution for simulating complex unsteady flows by filtering the flow with Sub-Grid Scale (SGS), solving the large eddies that are dominant terms of the turbulence spectra and handling the smallest eddies by SGS models. This approach has been extensively studied and applied in swirling flows of gas turbine combustors to simulate dynamic swirling flow structures for isothermal flow[9,10] and predicting the emissions[11] in combustion cases. In all such

applications, the validation of LES codes is crucial. High quality experimental data with well defined boundary conditions are highly desirable for the computational community. However, few experimental data are available for multiple swirl flows, especially data covering velocity statistics, temperature distribution, emissions, and combustion dynamics. This study intends to provide laboratory data on a LDI multi-swirl low emissions combustor, TARS, with different inlet and outlet boundary conditions. To avoid complicated issues associated with spray combustion, data presented in this paper are limited to gaseous fuel combustion although tests on spray combustion have also been conducted.

Experimental Setup

The core of the low NO_x LDI combustor is the Triple Annular Research Swirler (TARS), which was developed by Delavan Gas Turbine Products (DGTP, a division of Goodrich Aerospace) in collaboration with General Electric Aerospace Engines (GEAE). TARS (Figure 1) features three air passages, each with an individual swirler. Different configurations of TARS can be designed by changing the swirlers---outer swirler α, intermediate swirler β, and inner swirler γ--- either to different swirling vane angles or different rotating directions, to form different swirling flow fields. The inner and intermediate swirlers are axial swirlers whereas the outer swirler is radial. Hereafter, the swirler configuration will be labeled with the swirler angle in the order of outer, intermediate and inner, and with "C" labeling the counter-rotating swirl direction. For example, S5545C45 means that the swirler configuration has 55° outer swirler, 45° intermediate swirler in counter-rotating direction and 45° inner swirler. The total length of TARS is 66 mm (2.6") and the diameter of the outer swirler exit is 50.8 mm (2"). The intermediate swirler is located 66 mm (2.6") upstream of TARS exit whereas the inner swirler is at 50.8 mm (2 ") upstream of TARS exit plane.

Two sets of distributed fuel injection circuits are integrated within the TARS assembly: pilot fuel circuit injects fuel inwards into the intermediate swirling air passage and the main fuel circuit injects fuel outwards into the outer swirling air passage. Gaseous fuel is injected through both the pilot and main fuel circuits. The number of injection holes for the pilot and main fuel is four and eight, respectively. All the injection holes are identical, 0.762 mm (0.03") in diameter. These injection holes are perpendicular to the wall so that the gaseous fuel is injected normal to the air streams.

The atmospheric combustion test rig with the TARS fuel injector is depicted in Figure 2. The rig consists of an inlet flange, flow conditioning chamber (609.6 mm =24" long), plenum chamber (361.9 mm =14.25" long), and the combustion chamber. The flow conditioning and plenum chambers are constructed of 6 inches schedule 80 stainless steel pipes with inner diameter of 133.4 mm (5.25"). Flowing through the flow conditioning chamber, the flow passes through a perforated cone and then through a sequence of 5 fine-mesh screens whose mesh size is gradually reduced to 0.05mm (0.002") diameter with 44% open area ratio. The fuel injector, TARS, is centered on a mounting plate (6.35mm=0.25" thick) and flush mounted with the combustor chamber inlet.

Two types of combustion chambers were utilized in this study. The first one is a 457 mm (18") long cylindrical quartz tube, with a 101.6 mm (4") inner diameter, and a 2.5 mm wall thickness. Data on the velocity statistics, flame images, and emissions were taken from tests performed with this cylindrical combustor. The second combustion chamber had an octagonal cross-sectional shape with three 5 mm thick flat quartz walls and one stainless steel wall that was instrumented with thermocouples. The cross sectional area of the octagonal combustor, whose dimensions are shown in Fig. 2c, is identical to the cylindrical one. Temperature measurements

8

were performed in the octagonal combustor because it provided optical access for flame imaging while avoiding difficulty of drilling thermocouple access holes on the cylindrical quartz tube. A short mixing tube (Fig. 2b) can be inserted between the TARS exit and the combustor dump plane. This mixing tube has the same inner diameter as the TARS exit. The total length of the mixing section, L, composed of the mixing tube, sealing gasket, and the mounting plate, is normalized by the diameter of the TARS exit, D, as $L_{mt}=L/D$. Figure 2d is the streamwise sectional view of the mixing section with $L_{mt}=0.5$. The combustion products exit the combustor through a circular exhaust nozzle (Fig. 2e). The contraction ratio is defined as the ratio between the exhaust nozzle and the combustion chamber areas, noted as C_R. The geometrical parameters of the experimental setup are summarized in Table 1.

The rig is set up vertically with the combustion air preheated by a 36 kW electric heater to the desired temperature flowing through the inlet flange into a flow conditioning chamber. Static pressure transducer (Druck PMP 4000 series, ±0.04% FS accuracy, 1 psi range) and type K thermocouple were mounted in this chamber to monitor the pressure drop, dynamics pressure oscillations, and inlet air temperature. The air mass flow rate was metered by a digital flow meter (Eldridge Prouducts, Inc, 1% accuracy). The gaseous fuel flow was set at 30 psi controlled by a needle valve and metered by a digital gas flow meter (Alicat M series, ±1% FS accuracy).

The gas sampling and analysis system was an extractive sample conditioning and control system, which provided a representative sample to a chemiluminescence NO_x monitor and an infrared CO monitor with an installed paramagnetic O_2 sensor. The system has a 10 ppb resolution for NO/NO_x, 0.1 ppm for CO, 0.1% for CO_2 and O_2. The sampling probe was heated to above 100°C to eliminate water vapor from the sample. The CO analyzer is designed to be in a serial arrangement using a pneumatic type differential sensor to minimize the interference from

CO_2 or water vapor. All process parameters, including main air flow rate (m_a), air inlet temperature (T_3), plenum pressure (p_3), pressure inside combustion chamber (p_4), combustion gas temperature (T_4), combustor wall temperature (T_w), total fuel flow rate (W_f), were recorded by Labview software, as well as the emissions data from the gas analyzer.

Stereoscopic PIV system was used to measure the velocity flow field inside the combustion chamber. The system included: two 120 mJ 15 Hz pulsed Nd-Yag laser (New Wave Research Gemini PIV laser Model 120-15), TSI PIV signal synchronizer, two 2048x2048 pixels12-bit Powerview CCD cameras, and two high performance frame grabbers. The 4 mm diameter laser beam from the laser head was spread by a cylindrical lens (Focal Length = -15mm or -25 or combination of two) and a spherical lens (Focal Length =500mm) into a laser sheet. The laser sheet was about 130 mm wide and 1mm thick at the location of the beam waist which overlapped the centerline of the combustion chamber.

For measurements in the streamwise plane (including the combustion chamber axis), the two CCD cameras were at the same side of the laser sheet with a separation angle of 30°, focusing on the field of view created by the pulsed laser sheet in the streamwise plane (r-z plane in Fig. 2a). Based on the displacement of pixels between the two laser pulses (in this experiment the laser pulse interval was between 6 μs to 12 μs), radial velocity (V_r) and axial velocity (V_z) were obtained with units of pixels per second. To obtain the tangential velocity component (V_θ), which was perpendicular to the laser sheet, a calibration procedure was applied to generate the correlation equation by imaging several (normally two) planes with different depth in the perpendicular direction.

A type B thermocouple (6%Rh/Pt-30%Rh, 10 mil lead wire) with ceramic insulation tube was mounted on a 2-D traverse system to map the temperature field. All temperature data were corrected for radiation effects using the equation[12].

$$T_g = T_{tc} + \varepsilon_{tc}\sigma(T_{tc}^4 - T_w^4)d / kNu \qquad (1)$$

Where,

Emissivity $\epsilon_{tc} = 0.22$;

Stefan-Boltzmann constant $\sigma = 5.67 \times 10^{-8}\ JK^{-4}m^{-2}s^{-1}$;

Bead diameter $d = 0.03" = 0.762mm$;

Thermal conductivity for air at 1450K: $k = 0.0924 W/m.K$,

Nusselt Number: $N_u = 5.05$ based on the bead diameter and evaluated at 1500 K air according to correlation[12]:

$$Nu_{d,sph} = 2.0 + 0.6\,Re_d^{1/2}\,Pr^{1/3} \qquad (2)$$

All flow meters in this study have accuracy of $\pm1\%$. For fuel/air equivalence ratio, which is defined as the actual fuel/air ratio relative to stoichiometric ratio. The error in the fuel and air flow rates contributed $\pm1.4\ \%$ using the root mean square method. The Reynolds number was calculated from the air mass flow rate at the fuel nozzle exit, fluids properties (density and viscosity) and geometry. Since the errors in fluid properties and geometry were small, the error in Reynolds number is estimated to be 1%. Inlet air temperature was measured by type K thermocouples with $\pm1°C$ accuracy. The combustion temperature was measured with a type B thermocouple and precision thermometer with accuracy $\pm0.1°C$.

Results and Discussions

Vortex breakdown in ducted swirling flows, such as in the present combustion chamber, causes the formation of a central recirculation zone (CRZ), with reversed flow near the axis. This CRZ is either of spherical or spiral shapes, depending on the swirl strength and inlet flow Reynolds number. Swirling flows are three-dimensionally unsteady, and their dynamics are sensitive to geometrical factors. In the present study, the velocity statistics, velocity spectra, temperature distribution, OH* chemiluminescence images, and emissions characteristics are first presented for the baseline case (defined below). Following that, the effects of the inlet mixing tube length (L_{mt}) and the contraction of the combustor exhaust nozzle (C_R) on the swirling flow field, temperature distribution, and emissions are presented and discussed. The coordinates were normalized by the TARS exit radius, R=25.4 mm.

1. Baseline case

The baseline is a co-swirling case, with swirler geometry of S554545, in which all three swirlers are in the clockwise direction when observed from the upstream direction. There is no mixing tube (L_{mt}=0), and no exhaust nozzle contraction (C_R=1), i.e., the combustion chamber is not constricted at the exit.

a. Velocity field:

The non-reacting cold flow field is characterized first, followed by a gradual increase of the inlet air temperature to study the effect of temperature, and finally the velocity statistics for stable and unstable combustion are evaluated.

Velocity field of non-reacting swirling flows

The mass flow rate, the pressure drop across the swirler, and the inlet air temperature for the tests of non-reacting flow and reacting flow are listed in Table 2. The mass flow rate was kept constant for the cold, isothermal, and reacting flow cases. Inlet air temperature, T_3, is a major factor for gas turbine combustion performance therefore knowledge of its effects on a swirling flow field is necessary for combustor design and combustion performance improvement. For the same air mass flow rate, high temperature increases the bulk velocity and viscosity, significantly changing the inlet Reynolds number and potentially affecting the swirling flow dynamics.

Figure 3 shows the contours of normalized axial, tangential, and total turbulence velocity inside the circular combustion chamber for $T_3 = 23$ to 300°C. Axes r and z are in the radial and axial directions, respectively, as shown in Fig. 2a. V_r, V_z, and V_θ are the radial, axial, and tangential velocity components, respectively. Because V_θ is the out-of-plane circumferential component, its direction is opposite on the two sides of the centerline as shown with contrasting colors in the contour plot. The total turbulent kinetic energy (TKE), k, is defined as the sum of the squares of the three velocity components' fluctuations as $k = \frac{1}{2}(\overline{V_r'^2} + \overline{V_z'^2} + \overline{V_\theta'^2})$. Since the mass flow rates were kept constant, m_a=0.032kg/s, the average TARS exit velocity, V_0, was calculated from the volumetric flow rate as: 13, 16, 21, 25 m/s for $T_3 = 23$, 100, 200, and 300°C, respectively. The velocity components, V_z and V_θ, and the TKE, k, were normalized with V_0 as V_z/V_0, V_θ/V_0, and k/V_0^2. From the contours of V_z/V_0, it can be seen that the central recirculation zone (CRZ) has approximately a spherical shape for all the velocity fields in the temperature range $T_3 =23$ to 300°C, as indicated by the blue color in these plots. The width of the CRZ is ±0.6R at the exit of TARS (z/R=0.1) and increases to ±1.3 R at z/R=1.5. Further downstream, the CRZ's size reduces. Outside the CRZ is the region of an annular jet that emanates from the

swirler, as represented by the red and orange colors. In the present paper, this region is noted as the swirling jet in contrast to the CRZ region. The specific characteristics of the mean velocity field were also shown in the contours of V_θ/V_0 with low V_θ near the centerline at r/R=0 and a high V_θ region near z/R=3, r/R=1. The contours of k/V_0^2 depict the distribution of the total turbulence: the turbulence is strongest at the shear layer between the swirling jet and the CRZ and is lower inside the CRZ. The turbulence intensity in the shear layer is more than twice the level in the CRZ.

To quantify the observations from these contours, the profiles of V_z/V_0, V_θ/V_0, and k/V_0^2 at z/R=0.5 of Figure 3 are compared in Figure 4. The similarity of mean velocity distribution inside the CRZ is obvious in the profiles of V_z/V_0 and V_θ/V_0. For T_3 =23 to 300°C, the zero V_z/V_0 is located at ± 1R (Fig. 4a) and the vortex core (solid body rotation region) is between ±0.5R (Fig. 4b). It should also be noted that the profiles are scattered in the swirling jet region (beyond ± 1R in both Fig. 4a and 4b). Inlet temperature affected the turbulent velocity, k/V_0^2, particularly in the core (±0.5R) and in the jet region (beyond ± 1R). In summary, the mean velocity field preserved its characteristics with the increase of T_3, but the magnitude of the velocity components was significantly different because the bulk velocity increases whereas the mass flow rates were kept constant.

Velocity field of the reacting swirling flows

The velocity field of the reacting swirling flow differs from the isothermal one as a result of the changes in the temperature and the density due to the combustion heat release. The operating parameters of mass flow rate, pressure drop, and inlet temperature of the present measurements are listed in Table 2. It should be noted that at the same inlet temperature and mass flow rates, the pressure drop is considerably higher for unstable combustion compared to the stable case. A

14

comparison of V_z/V_0 and k/V_0^2 for isothermal, stable, and unstable combustion flows is shown in Figure 5. V_0 is 23 m/s at T_3=230°C. The central recirculation zones for all three cases had a spherical shape but were quite different in size and location relative to the swirler exit. For stable combustion, the CRZ is lifted and the constriction near the swirler exit (z/R=0) becomes significantly smaller, only ±0.2R compared to ±0.7R for the isothermal case. When unstable combustion occurred, the CRZ reduced in size from a 3R wide and 3.5R long sphere for the isothermal case to a compact region with 2R width and 2.5R length, and a significantly increased level of reversed axial velocity. In addition, the unstable combustion also caused asymmetric distribution of V_z at the left and right sides of the flow surrounding the CRZ (Fig.5a: Unstable Combustion Flow). Combustion dramatically affects the distribution of k/V_0^2, breaking the clearly defined low and high turbulence velocity regions of isothermal flow into dispersed form in the combustion cases (Fig. 5b).

To quantify the effect of combustion on the swirling flow fields, profiles of V_z/V_0, V_θ/V_0, V_r/V_0, and k/V_0^2 were extracted at z/R=0.2 of Fig. 5 and shown in Fig. 6. Compared with the isothermal case, the stable combustion forms much weaker recirculation flow at z/R=0.2 due to the downstream shift of the CRZ (Fig. 6a), but with fairly similar V_θ/V_0 radial distribution (Fig. 6b). Unstable combustion causes stronger reversed flow (negative V_z) within ±1R (Fig. 6a) and enhanced V_θ near ±1.5R (Fig. 6b) compared to the isothermal and stable combustion cases. Combustion, either stable or unstable, greatly enhances the radial motion of the swirling flow to about twice that of the isothermal case (Fig. 6c at r/R=±1). In terms of turbulent energy, in the vicinity of the nozzle exit, k/V_0^2 was similar for the stable combustion and isothermal cases (Fig. 6d); the unstable combustion, however, nearly doubled the magnitude of TKE relative to the isothermal and stable combustion cases in the range ±1R (Fig. 6d).

Spectra of velocity in the swirling flow

Information on the spectra of velocity fluctuations in turbulent swirling flows is important for properly modeling them. Constant temperature anemometer was used to measure the spectra of the confined turbulent swirling flow in the circular combustion chamber. The frequency was normalized by the TARS exit diameter D according to the following equation:

$$S_{tD} = \frac{fV_0}{D} \tag{3}$$

Where, f is the frequency in Hz.

For the spectral measurements, the single straight wire was oriented perpendicular to V_z and V_θ velocity components and parallel to the V_r component such that the spectra represented fluctuations of both V_z and V_θ. Figure 7 depicts the power spectra of V_z and V_θ at three axial locations z/R=0, 5, 10 along the shear layer at a constant radial distance of r/R=0.4. For reference, Kolmogorov $K^{-5/3}$ law is included. The high frequency broad band peak at a frequency of S_{tD}=3.3 which is present in the initial jet shear layer, disappears immediately downstream. Next to the vortex breakdown region, at z/R=5, the spectra has two peaks, S_{tD}=0.16 and 0.35. The second peak falls within the range of the jet preferred mode, S_{tD}=0.24-0.64, as described by Schadow and Gutmark for flow in dump combustors[13]. This frequency may also be related to the flow dynamics of the Precessing Vortex Core (PVC) associated with vortex breakdown, as suggested by Chao et al[14] in the study of spectral characteristics of swirling flow fields. The lowest frequency, S_{tD}=0.16, dominated most of the swirling flow except in the proximity of the TARS exit. The amplitude of this low frequency mode is amplified in the downstream direction. At z/R=10, the flow is dominated by this low frequency as is evidenced by the narrow band peak. Similar observations were made in the study of Chao et al.[14], who found a dominant low frequency in the downstream of swirling flow and classified it to be "most amplified downstream

azimuthal instability" and to be a strong function of the inlet Reynolds number and a weak function of swirl strength. It should be noted that beyond S_{tD}=0.5 the spectra at z/R=5 and 10 are following the $K^{-5/3}$ slope, indicative of a fully developed turbulence.

b. Temperature distribution

The radial distribution of the reacting flow temperature, T_4, was measured using a fine type-B thermocouple at four axial locations z/R=2, 4, 6, and 8. The symmetry of the radial temperature profile (defined as $\dfrac{(T_1 - T_2)}{(T_1 + T_2)/2}$, where T_1 and T_2 represent temperatures at two radially equidistant locations) was in the range of 0.3%-1%. Therefore, only half of the temperature field is shown. The combustion gas temperature was normalized with the temperate at the centerline, T_{CL}. Figure 8 shows the radial temperature profiles for propane at an equivalence ratio, Φ=0.57, and T_3=230°C. The overall temperature distribution is quite uniform in the main combustion region of r/R = 0 to 1.5 over an axial extent of z/R = 2 to 8. The temperature drops rapidly near the wall. Since the fuel spreads outwards with the conical swirling air jet, the flame has also a conical shape as indicated by the temperature distribution.

c. OH* chemiluminescence image

It is commonly accepted that CH* and OH* chemiluminescence represents reaction or heat release rate if the integrated chemiluminescence is linearly related to fuel consumption and the electronically excited radicals are confined to a relatively thin region in the vicinity of the primary flame surface[15]. The primary source of OH* ($A^2 \Delta$) is believed to be produced by oxidation of CH with transition around 308 nm. For overall flame structure characterization, the chemiluminescence image was taken with 10 ms exposure time. A band pass filter centered at 308 nm was used to cut off interference from other radical emissions.

17

Figure 9 is the OH* image at $\Phi=0.57$, $T_3=230°C$ for baseline case. The color bar is the pixel value normalized by the background level. The flame was centered along the four air streams that emanated from the swirler through the four vanes. Because the chemiluminescence is a line-of-sight integration the intense flame located near the center is actually an overlap of the two front and aft flame sections. LDV measurements and 3-D Reynolds Averaged Navier-Stokes simulations showed that the flow in the cross-sectional plane is azimuthally asymmetric[16]. Air flowing through the vanes of the intermediate and outer swirlers has higher velocity and forms high velocity regimes at the TARS exit plane. The number of high velocity air streams matched the four vanes in the intermediate swirler. In a computational effort it is necessary to include the mixer-swirler in the computational domain in order to capture the azimuthal asymmetry of the reacting swirling flow.

d. Emission characteristics

Formation of emissions is a result of a combined effect of the swirling flow field, the fuel distribution, the reaction characteristics and the temperature distribution. Figure 10 shows the NO_x emissions and calculated adiabatic equilibrium temperature at $T_3=230°C$. The NO_x is corrected to 15% O_2 value according to the equation:

$$(NO_x)_{15\%O2} = (NO_x)_{measured} \times 5.9/(20.9 - O_{2,measured}) \qquad (4)$$

The adiabatic equilibrium temperature was calculated using the NASA CEA code. Formation of NO_x increases with the fuel equivalence ratio and the flame temperature. The baseline multi-swirler design of this LDI combustion system has low NO_x emissions in a range of 4 to18 ppm for Φ of 0.55 to 0.81.

2. Effect of inlet boundary conditions

The swirling flow is very sensitive to inlet boundary conditions as are combustion properties, including dynamics and emissions, which are closely related to the flow field characteristics. As stated in the experimental setup section, a short mixing tube can be inserted between the TARS exit and the combustion chamber to convert the LDI arrangement to a premixed combustion configuration. This mixing tube not only provides additional volume for premixing fuel and air but also has significant impact on the swirling flow field and the combustion process. The length of this mixing tube (L_{mt}) is an important inlet boundary condition for properly simulating complex non-reacting or reacting swirling flows. This section will emphasize the effect of the mixing tube length on the velocity profiles, velocity spectra, temperature distribution, and emissions.

Figure 11 depicts the comparison of profiles of V_z/V_0 and V_θ/V_0 at z/R=0.4 for L_{mt}=0, 0.3, 0.55, and 0.8. When L_{mt} increases, the upstream stagnation point of the vortex breakdown region moves upstream into the mixing tube. The mixing tube increases V_z and V_θ velocity components of the downstream swirling jet surrounding the CRZ (Fig. 11a & b) and enhances the magnitude of the reversed flow (Fig. 11a). Close to the combustor inlet, the mixing tube formed a larger vortex core region extending to r/R=±1 (Fig. 11b) compared to the case without the mixing tube where it extends only to r/R = ±0.5. The 3-D vector field plot (Figure 12) shows a pair of large vortical structures, which did not exist for L_{mt}=0, that was nested along the rolling flow structure for L_{mt}=0.55. These large vortices were also observed for L_{mt}=0.3 and 0.8, and their location moved upstream with increased L_{mt}[17]. Since the PVC structure is less likely to be damped in premixed combustion[18], these vortices can potentially be responsible for the excitation of combustion dynamics.

The velocity spectra of L_{mt}=0.55 (Fig. 13) shows three frequency regimes along the swirling flow shear layer. The high frequency (S_{tD}=0.67) is located in the initial shear layer of the swirling jet (z/R=0) and the low frequency (S_{tD}=0.15) is located further downstream (z/R=10). Compared to the high frequency S_{tD}=3.3 of L_{mt}=0, the high frequency of L_{mt}=0.55 is much lower. Since with a longer mixing tube the combustor acquires features of dump combustor geometry, the high frequency may be related to the most amplified initial shear layer frequency as found in dump combustors. The intermediate frequency (S_{tD}=0.37), which is the secondary peak of L_{mt}=0 at z/R=5, becomes the dominant frequency along the vortex breakdown region, suggesting that the mixing tube promotes stronger dynamics of the vortical structures observed in the 3-D vector plot (Fig. 12). For L_{mt}=0.55, the -5/3 slope appears in the spectra between S_{tD}=0.5 to 2 and the spectra of higher frequency has an even higher slope, indicating reaching a fully developed turbulence and stronger dissipation at high frequencies compared to the L_{mt}=0 case in Figure 7.

Figure 14 depicts the flame OH* chemiluminescence for L_{mt}=0.5 and a comparison between the temperature distribution of L_{mt}=0 and 0.5. Compared with the OH* image of L_{mt}=0 (Fig. 9), the insertion of the mixing tube stretched the flame, pulled it into the mixing tube, and reduced the flame lateral expansion. The temperature field showed very similar peak temperatures of >1600K for both L_{mt}=0 and 0.5, however, the region of high temperature is larger and is shifted towards the walls with the mixing tube. The NO_x emissions (Fig. 15a) were halved by the mixing tube for Φ = 0.6-0.76. The shorter residence time caused by the increased jet velocity of L_{mt}=0.5 is the key for NO_x reduction. Conversely, residence time affects the oxidation of CO, producing more CO for L_{mt}=0.5 than L_{mt}=0 (Fig. 15b). The mixing tube has an adverse effect on the flame stability, shifting the equivalence ratio of LBO (Φ_{LBO}) from Φ_{LBO} =0.52 for L_{mt}=0 to Φ_{LBO} =0.6 for L_{mt}=0.5. This is a result of the flame with the configuration that

includes the mixing tube being stabilized primarily by the CRZ stagnation region, while with no mixing tube the flame is also stabilized by the dump plane recirculation zone.

3. Effect of outlet boundary conditions

Experimental studies[14,19] regarding the effect of the exhaust area contraction ratio (C_R) on the shape of the CRZ have shown that the downstream boundary conditions at the exhaust nozzle can affect the upstream flow field if the flow remains in a subcritical state after vortex breakdown. However, these studies were limited to non-reacting flows. To emphasize the importance of exit boundary conditions of the combustor, which are sometimes neglected in computational studies, this section addresses the significant influence of downstream exit conditions on non-reacting and reacting flows.

The contours of V_z/V_0 component for C_R =4 (Fig.16) illustrates the effect of the downstream contraction on CRZ: the shape of CRZ (blue color in the contour plot) changed from a spherical shape (Fig.3 V_z/V_0) of C_R=1 to a conical "V" shape for large contraction ratio of C_R=4. The larger contraction ratio caused the recirculation zone to collapse near the centerline, forcing the reversed flow to recover back to the downstream direction and moved the location of downstream stagnation point from z/R=4 for C_R=1 to z/R=0.5 for C_R=4. Profiles of V_z/V_0 at z/R=2 for C_R=1.14 to 4 (Figure 17a) clearly depict the recovery process of reversed flow at the central flow region (negative V_z) within r/R=±1. Outside this region, profiles V_z/V_0 remain unchanged for all C_R. The V_θ component (Fig. 17b) shows that the split of the recirculation zone in the central region for large nozzle constriction results in a 50% increase in the magnitude of this component as C_R changes from 1.14 to 4. This is accompanied by an increase in the radial slope of the V_θ velocity in the vortex core region. Large contraction of the combustor exit introduces a transformation in the CRZ shape and a stronger rotation of the vortex core.

Velocity spectra provided additional information on the effect of the downstream contraction. Figure 18 presents the velocity spectra of V_z and V_θ components for C_R=4 at a fixed radial location, r/R=0.4, at three axial locations along the shear layer of the swirling flow: z/R=0, 5, and 10. A comparison of these spectra with those corresponding to the baseline case shows that:

1) High frequency velocity fluctuations, S_{tD}=3.2, are still dominant close to the TARS exit (z/R=0). The Strouhal Number of the high frequency remains nearly the same for C_R=1 and 4 and is not affected by the exhaust nozzle contraction ratio.

2) The low frequency of S_{tD}=0.15 at z/R=10 is less dominant for C_R=4 than for C_R=1, indicating the dampening effect of the contraction on this low frequency in the downstream flow region.

3) The middle range frequency of S_{tD}=0.37 is amplified for large contraction. This frequency is located at the inner shear layer formed between the recovered downstream flow and the reversed flow at the vicinity of the burner axis. Therefore, it is proposed that the downstream contraction augments the precessing vortices in the central vortex breakdown region. For z/R>5 the turbulence spectra reaches a fully developed state as indicated by the -5/3 slope.

The comparison of NO_x emissions and temperature distribution for C_R=1 and C_R=4 is shown in Fig. 19. In the present case, for gaseous fuel with high inlet air temperature, NO_x increased exponentially with the lean equivalence ratio (i.e., with flame temperature), following the same trend line for both contraction ratios over the range of Φ = 0.54 to 0.75. OH* chemiluminescence showed that the flame structure of the two cases was nearly identical[20]. The temperature fields of the two contraction ratios showed nearly uniform distributions with temperatures ranging from 1550-1600K. These results suggest that the flame structure and the emissions characteristics were not sensitive to the downstream contraction ratios for gaseous fuel

for this specific combustor geometry. This observation confirms the hypothesis suggested by Escudier and Keller[19] that the subcritical state observed in cold vortex breakdown tests may disappear in combustion. The fast expansion which increases the axial velocity, and the stronger viscous effects resulting from the elevated temperature field, promote transition from sub-critical to supercritical state upstream of the combustor exit.

The results are different for liquid spray combustion for different contraction ratios. Figure 20 shows the NO_x emissions and temperature distribution for $C_R=1$ and 4 with ethanol fuel. NO_x level for $C_R=4$ was almost twice higher than that of $C_R=1$. Regarding the temperature contours, the large contraction increased the peak temperature from 1707K for $C_R=1$ to 1829K of $C_R=4$ and the high temperature region was significantly enlarged. The temperature field was also affected by the V shaped CRZ induced by the large contraction. In this case, properly modeling the downstream contraction is vital for an accurate computational simulation.

Conclusions

The present study investigated the detailed 3-D swirling flow velocity statistics, temperature distribution, OH* chemiluminescence, and NO_x and CO emissions characteristics of a multi-swirl low NO_x combustor. This experimental study emphasized the significant impact of inlet and outlet boundary conditions on the non-reacting and reacting flows.

Increased air inlet temperature enhanced the magnitude of reversed flow in the central region, increased the tangential velocity in the swirling jets, and the energy of the turbulent velocity fluctuations. These effects can contribute to the typical NO_x increase with higher inlet air temperatures and can be explained in terms of enhanced reaction and heat release rate, and increased residence time.

An addition of a mixing tube in the combustor inlet did not only serve as an additional mixing volume for fuel and air, but also led to aerodynamic changes of the swirling flow field. It had an effect on the magnitude of the axial and tangential mean velocity components, and on the formation of large vortical structures in the CRZ. NO_x emissions were substantially reduced with the mixing tube due to these effects, but increased CO production and reduced flame stability were observed.

The contraction ratio of the combustor exhaust nozzle transformed the shape of the recirculation zone from a spherical shape to a conical recirculation zone and greatly increased the tangential velocity inside the vortex core. Although NO_x formation for different contraction ratios were comparable with gaseous fuel, the dramatic influence on the temperature distribution and NO_x emissions of liquid spray combustion, emphasizes the importance of downstream boundary conditions.

Table 1: Geometrical parameters of the atmospheric combustion test rig.

Combustor diameter (cylindrical type)	101.6 mm (4"), D_C
Combustor inlet diameter	50.8 mm (2"), 0.5 D_C
Inner diameter of fuel injection hole	0.76 mm (0.03")
Length of cylindrical combustor	476 mm (18"), 4.5 D_C
Length of octagonal combustor	476 mm (18"), 4.5 D_C
Intermediate swirler location from the combustor inlet plane	66 mm (2.6"), 0.65 D_C
Inner swirler location from the combustor inlet plane	50.8 mm (2"), 0.5 D_C
Outer swirler cone diameter	50.8 mm (2"), 0.5 D_C
Length from the final stage screen to the combustor inlet	546 mm (21.5")

Table 2: Test conditions for non-reacting and reacting flows

	Mass Flow Rate (W_a, g/s)	Pressure Drop (Δp, psi)	Inlet Temperature (T_3, °C)
Cold flow case	32	0.425	23
Isothermal flow case 1	32	0.548	100
Isothermal flow case 2	32	0.623	200
Isothermal flow case 3	32	0.785	300
Isothermal flow case 4	32	0.76	230
Combustion flow (stable)	32	0.80	230
Combustion flow (unstable)	32	1.05	230
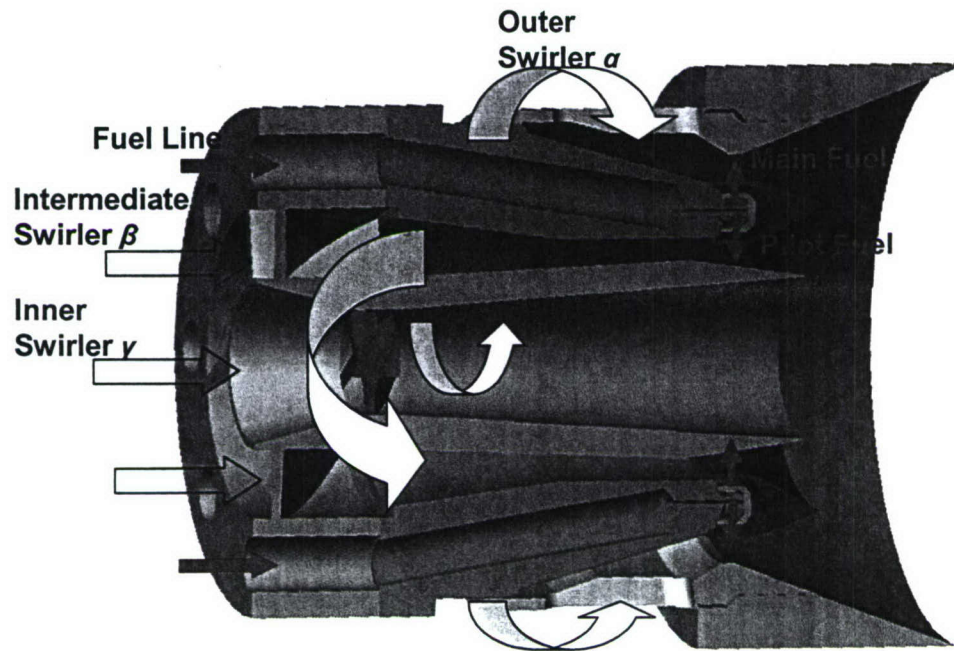
Figure 1: Section view of the Triple Annular Research Swirler.

(a) Test Rig

(b):3-D of mixing tube

(c) Cross section view of octagonal combustor

(d): Streamwise section view of mixing tube, L_{mt}=0.5.

(e): Section view of exhaust nozzle: C_R=4.
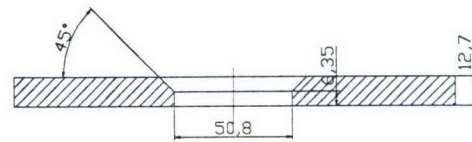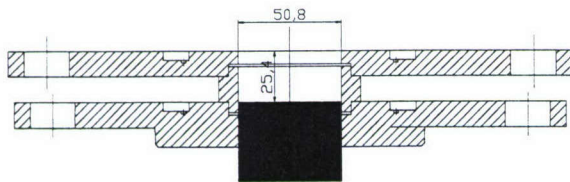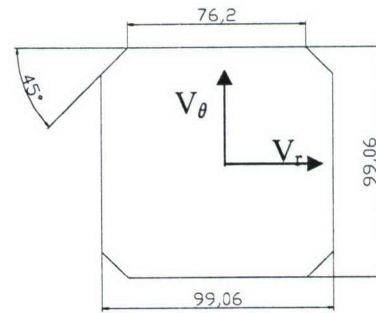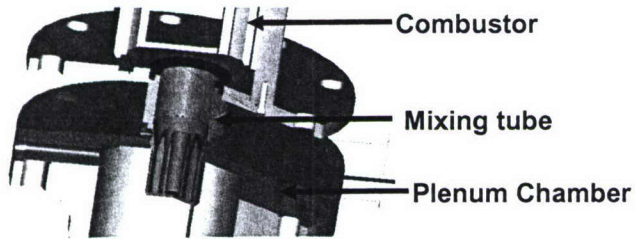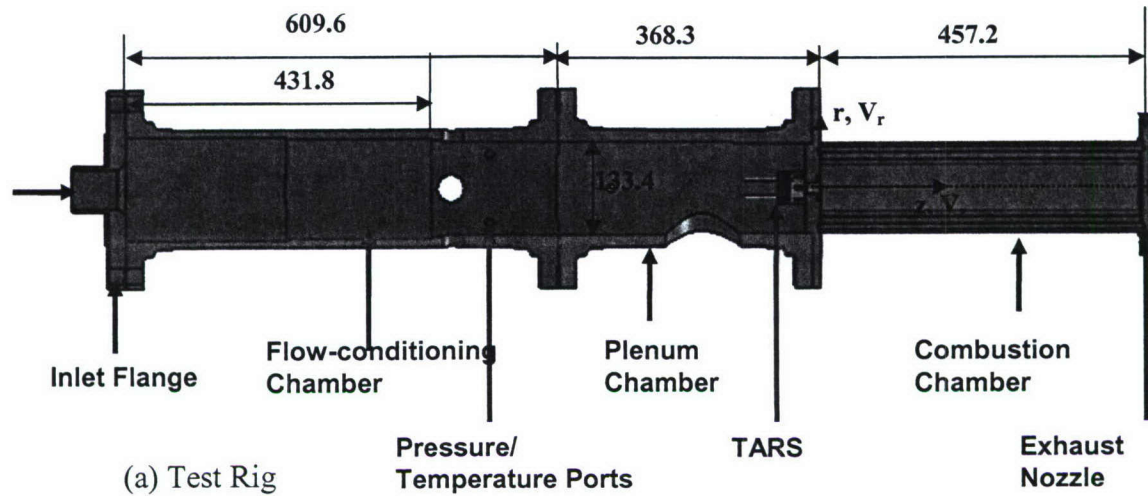
Figure 2: Drawings of the (a) Atmospheric combustion test rig of TARS, (b) 3-D mixing tube setup, (c) Cross sectional view of octagonal combustor, (d) Streamwise sectional view of mixing tube L_{mt}=0.5, and (e) Sectional view of the exhaust nozzle with C_R=4. All dimensions are in mm.

V_z/V_0 V_θ/V_0 k/V_0^2

T_3=23°C

T_3=100°C

T_3=200°C
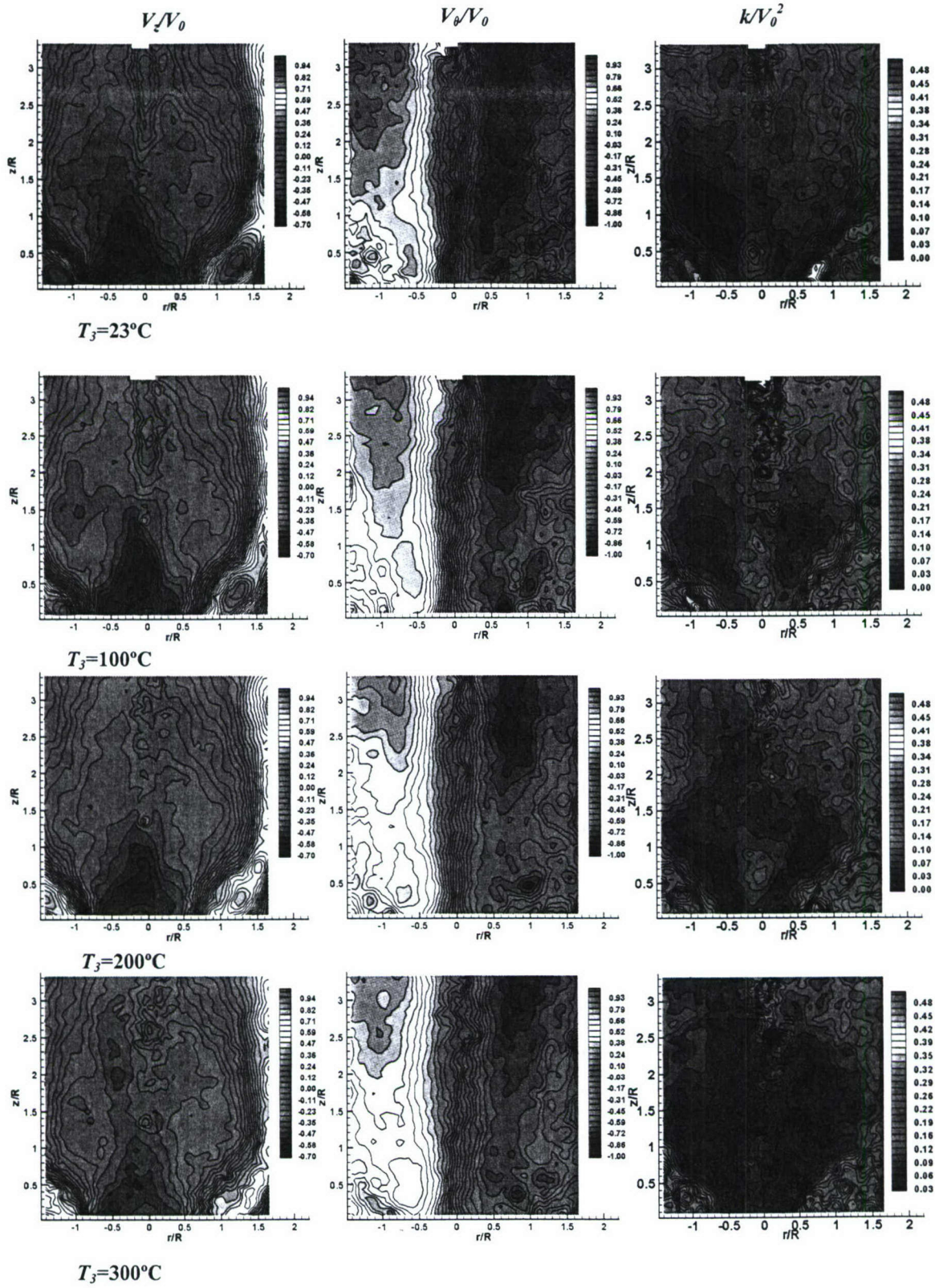
T_3=300°C

Figure 3: Contours of V_z/V_0, V_θ/V_0, and k/V_0^2 at T_3=23, 100, 200, 300°C: m_a=0.032kg/s, L_{mt}=0, C_R=1.

(a)

(b)

(c)
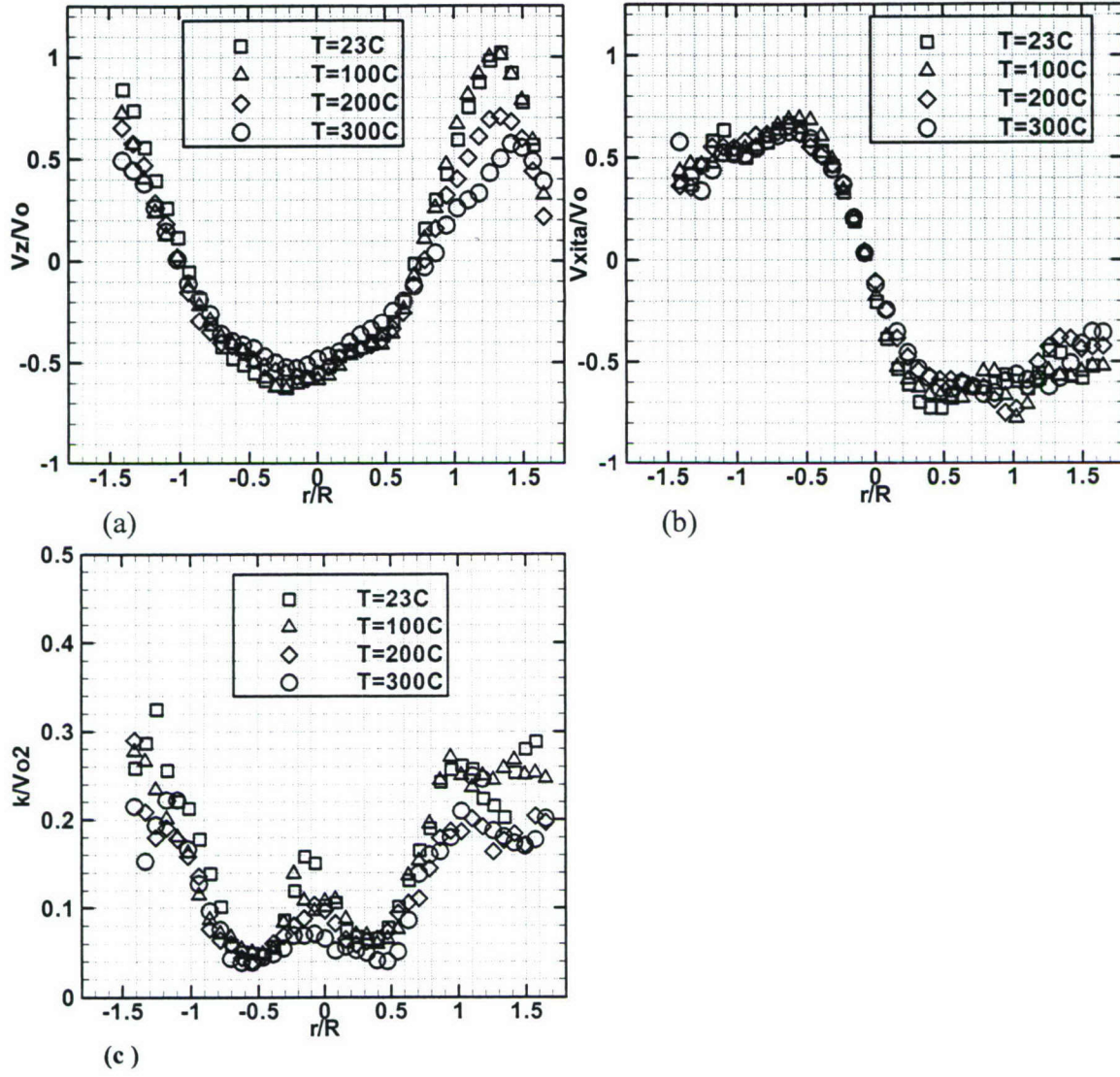
Figure 4: Profiles of (a) V_z/V_0, (b) V_θ/V_0, and (c) k/V_0^2 at z/R=0.5 for T_3=23~300°C, m_a=0.032kg/s, L_{mt}=0, C_R=1.

(a) V_z/V_0 and **(b)** k/V_0^2

Isothermal Flow

Stable Combustion Flow

Unstable Combustion Flow
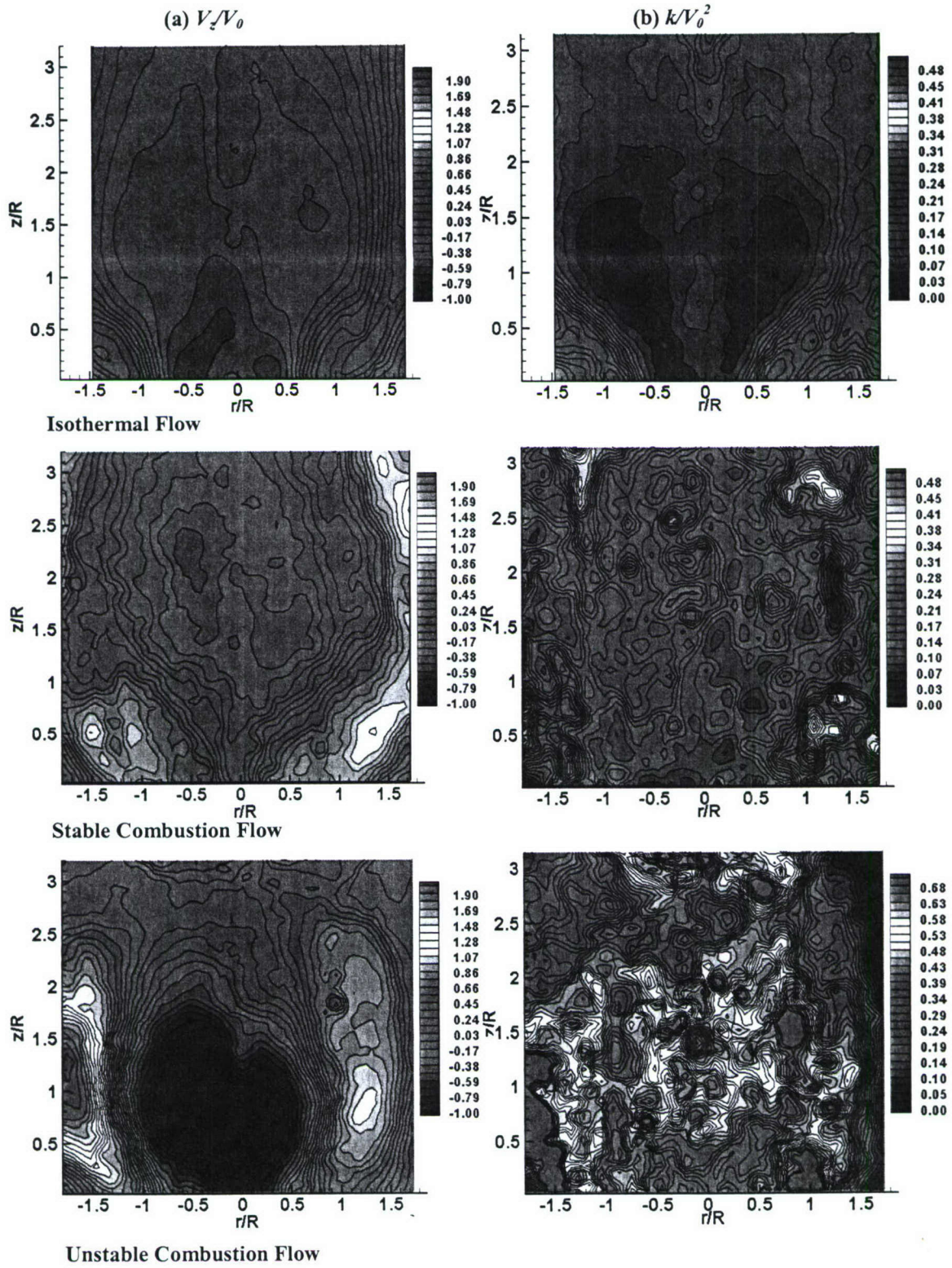
Figure 5: Comparison of contours of, (a) V_z/V_0 and (b) k/V_0^2 for isothermal, stable combustion, and unstable combustion flows: m_a=0.032kg/s, L_{mt}=0, C_R=1.

30
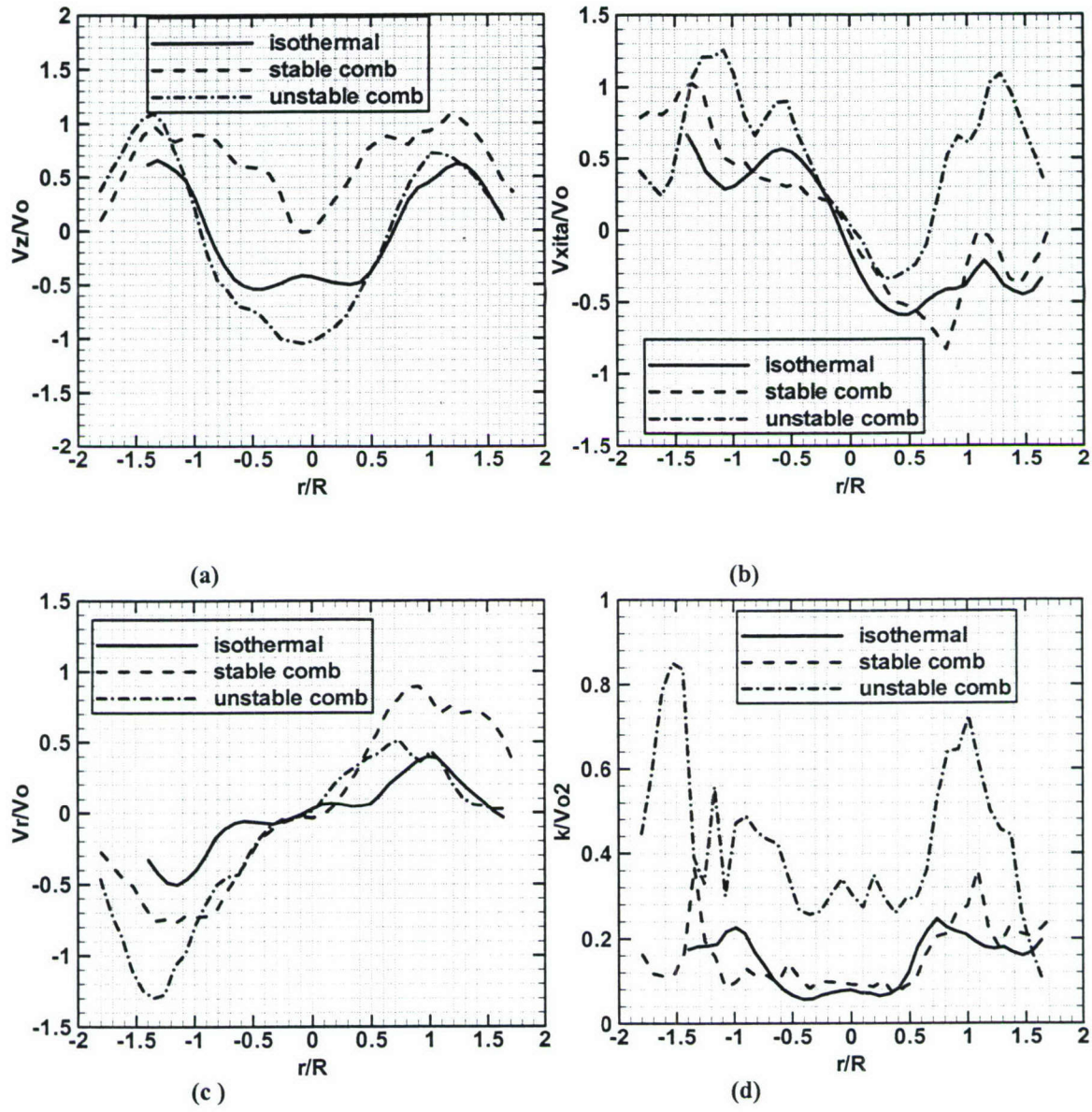
Figure 6: Comparison of radial profiles of (a)V_z/V_0, (b)V_θ/V_0, (c)V_r/V_0, and (d)k/V_0^2 at z/R=0.2 for isothermal, stable and unstable combustion cases. T_3=230°C, m_a=0.032kg/s, L_{mt}=0, C_R=1.
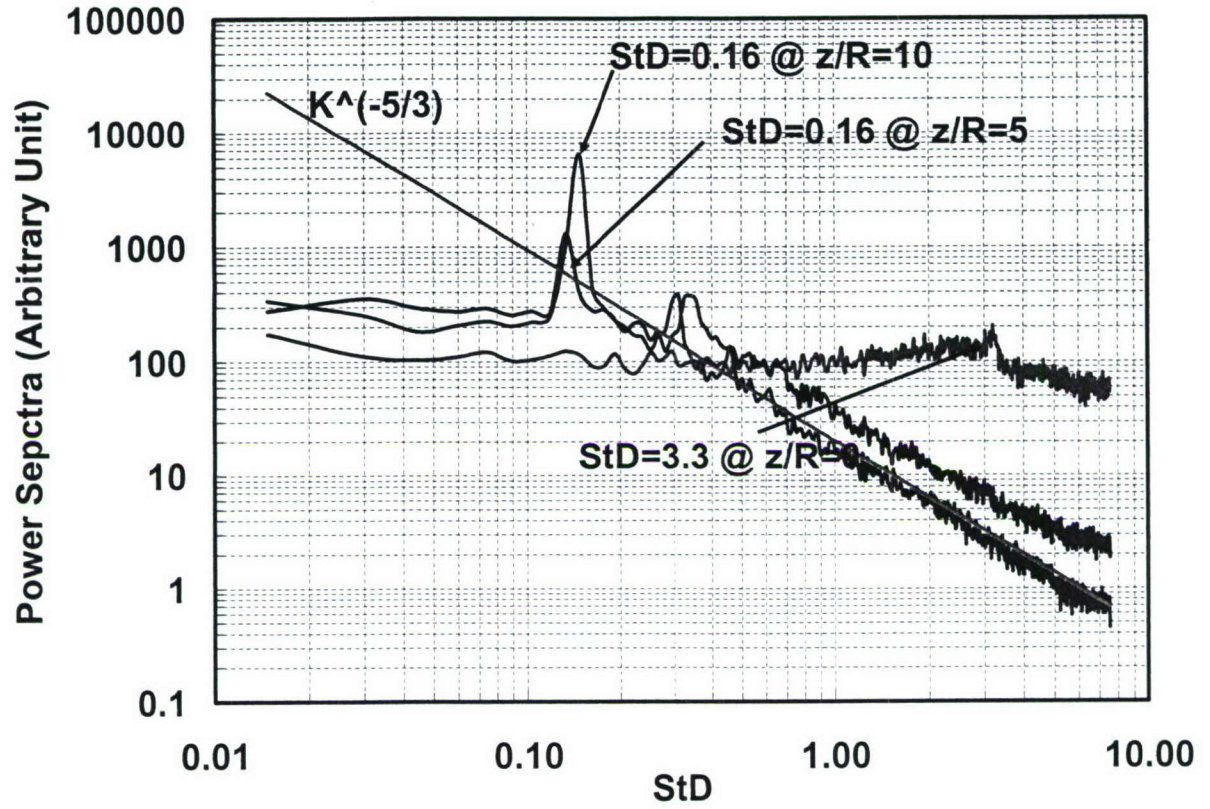
Figure 7: Spectra of velocity (combined V_z and V_θ components) at three locations of r/R=0.4 inside the swirling flow: m_a=0.032kg/s, T_3=23°C, L_{mt}=0, C_R=1.
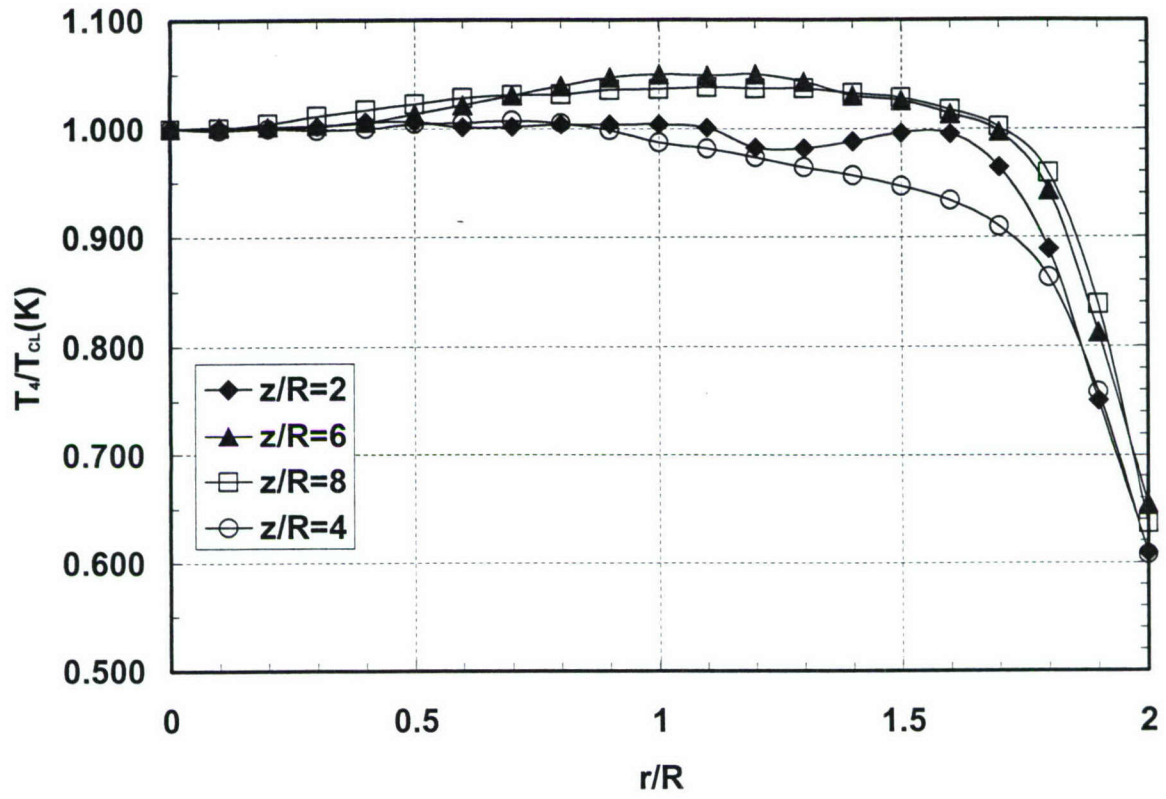
Figure 8: Radial profiles of T_4/T_{CL} at different axial locations: gaseous propane, Φ=0.57, m_a=0.022g/s, T_3=230°C, L_{mt}=0, C_R=1, octagonal combustor.
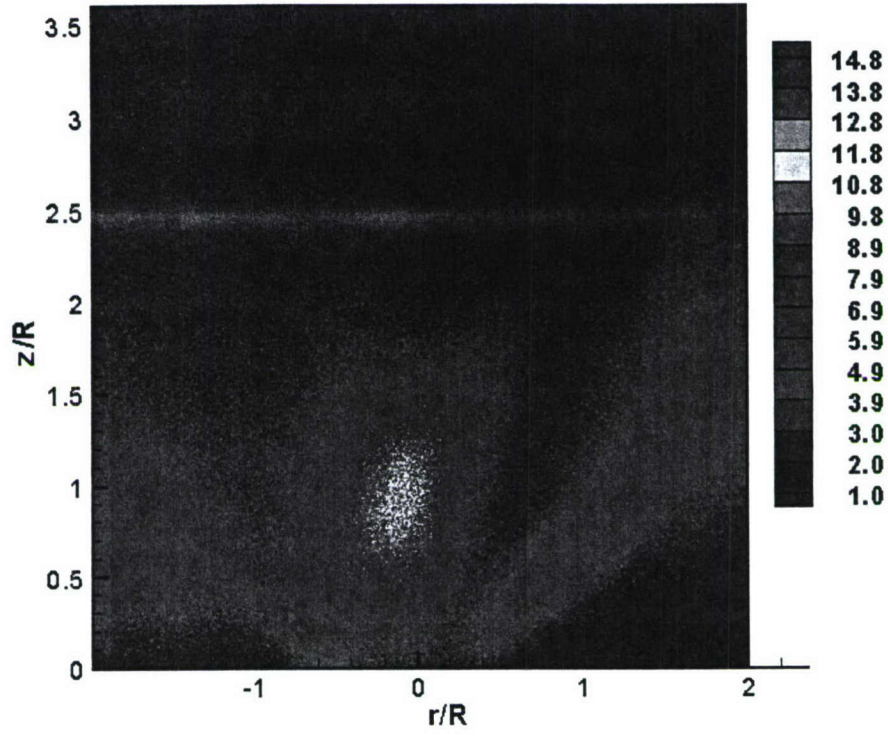
Figure 9: OH* chemiluminescence image for baseline case: Φ=0.57, T_3=230°C, m_a=0.032kg/s, L_{mt}=0, C_R=1.
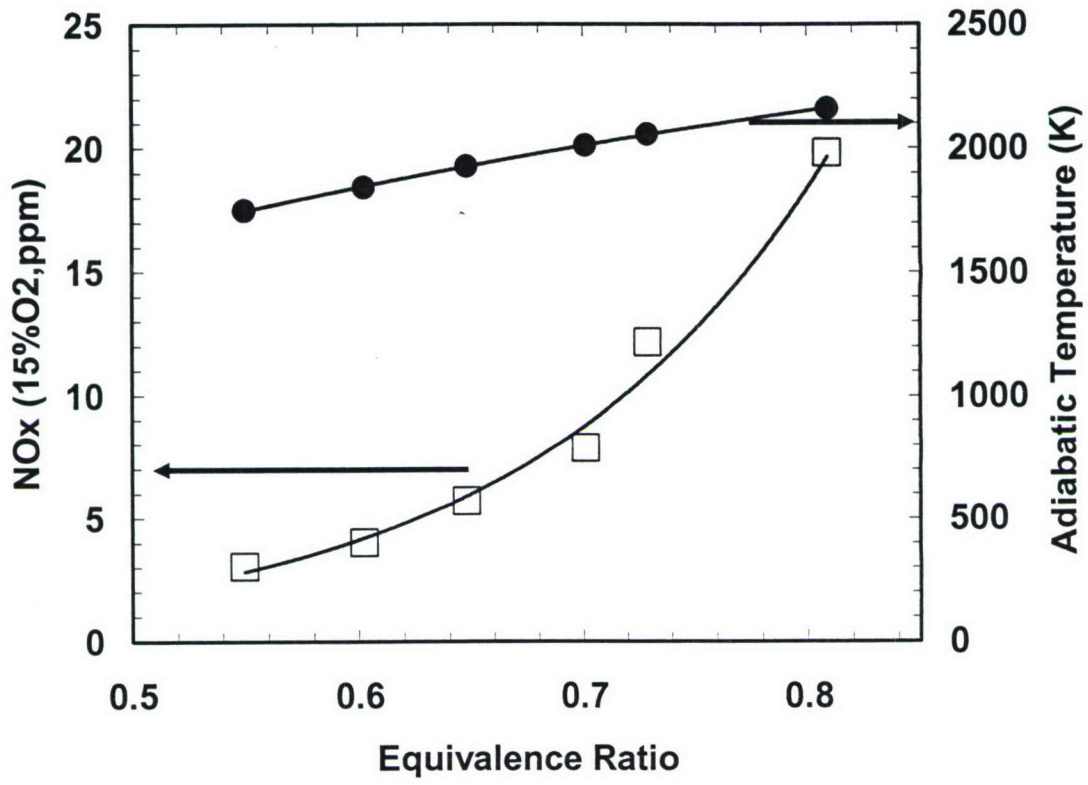
Figure 5: Dependence of NO_x emissions and adiabatic temperature on fuel equivalence ratio: m_a=0.032kg/s, T_3=230°C, L_{mt}=0, C_R=1, propane.
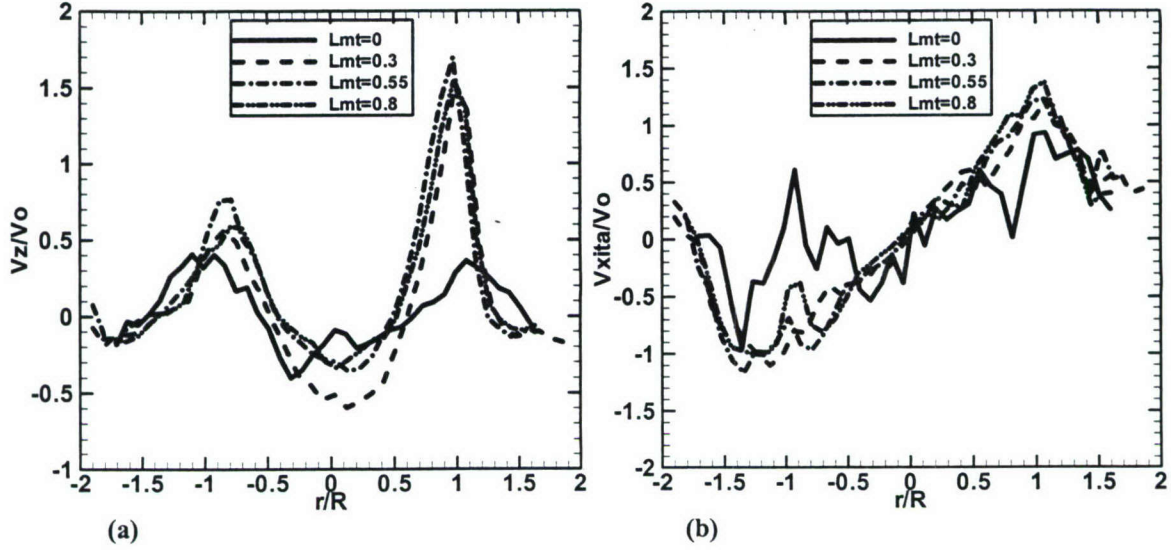
Figure 6: Comparison of profiles of (a) V_z/V_0 and (b) V_θ/V_0 at z/R=0.4 for L_{mt}=0, 0.3, 0.55, 0.8: m_a=0.032kg/s, T_3=25°C, C_R=4.

$L_{mt}=0$ $L_{mt}=0.55$
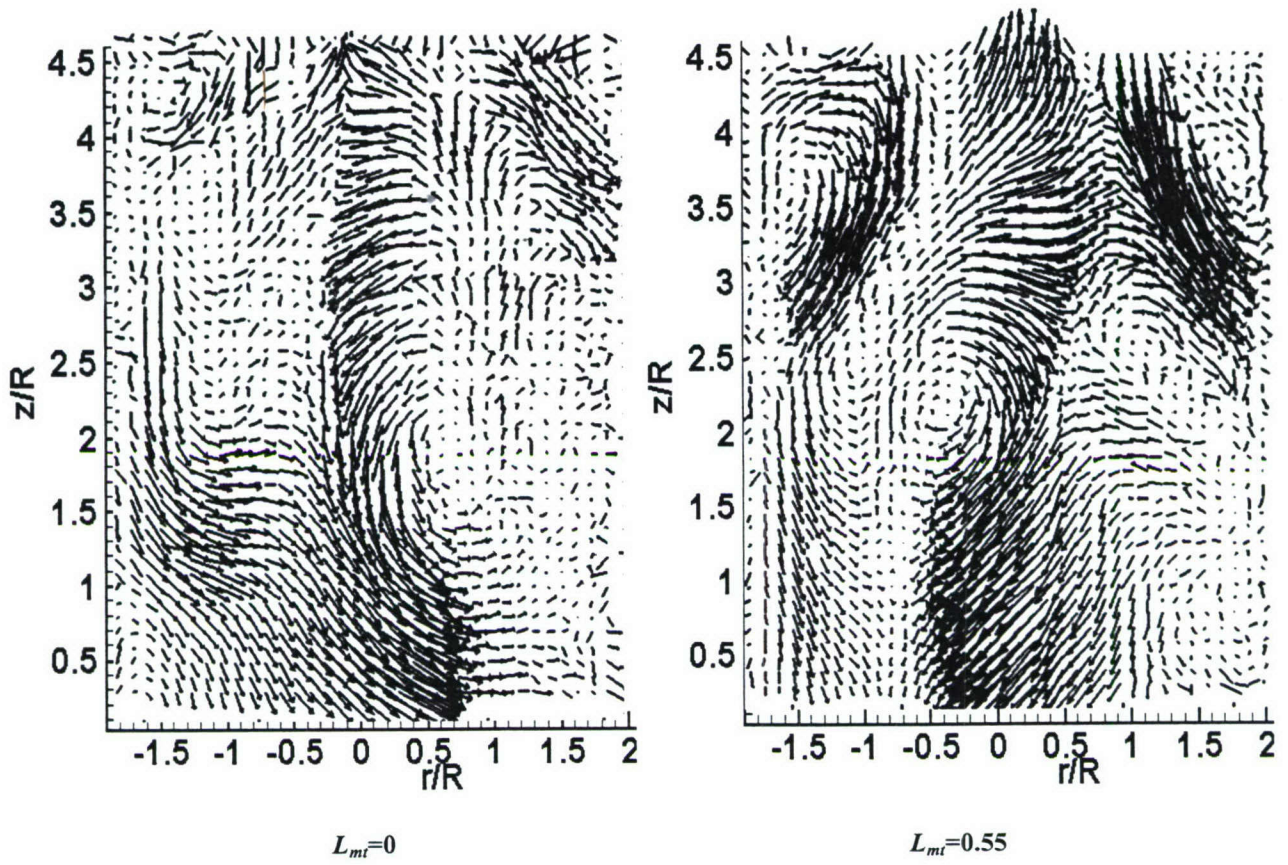
Figure 7: 3-D vector field for $L_{mt}=0$ and 0.55: $m_a=0.032$kg/s, $T_3=23$°C, $C_R=4$.
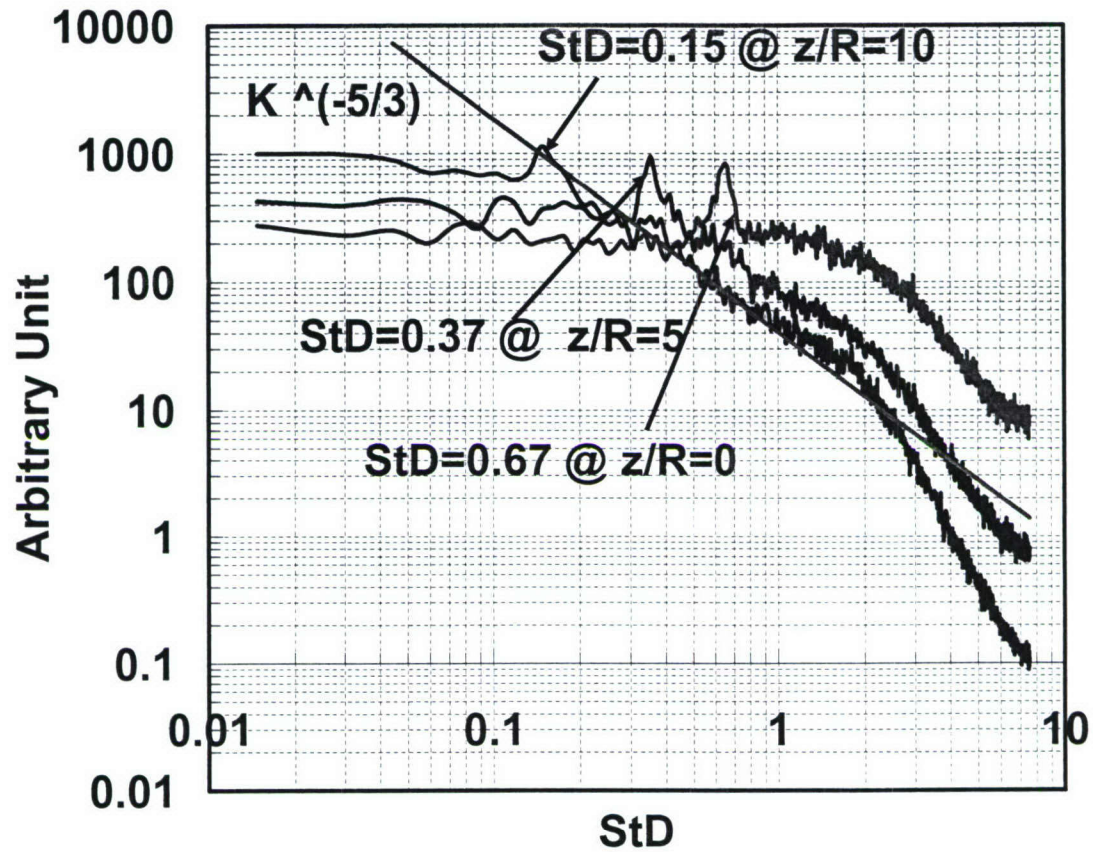
Figure 8: Spectra of velocity on three locations of r/R=0.4, z/R=0, 5, 10, inside the swirling flow: m_a=0.032kg/s, T_3=23°C, L_{mt}=0.55.
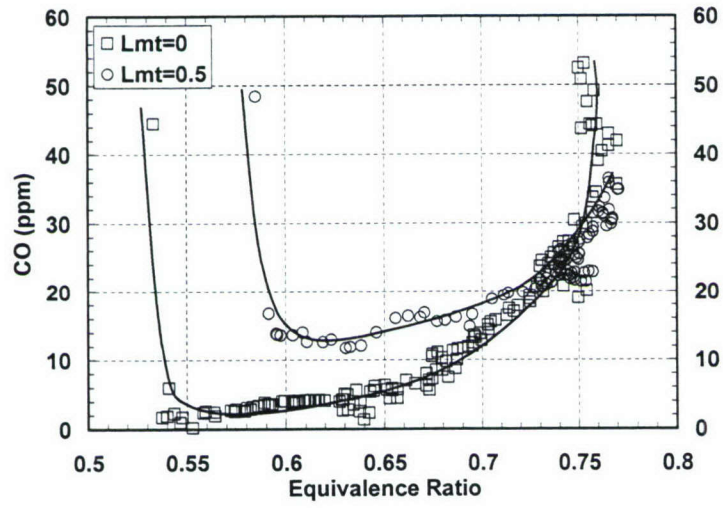
(a) OH* Chemiluminescence   (b) Temperature
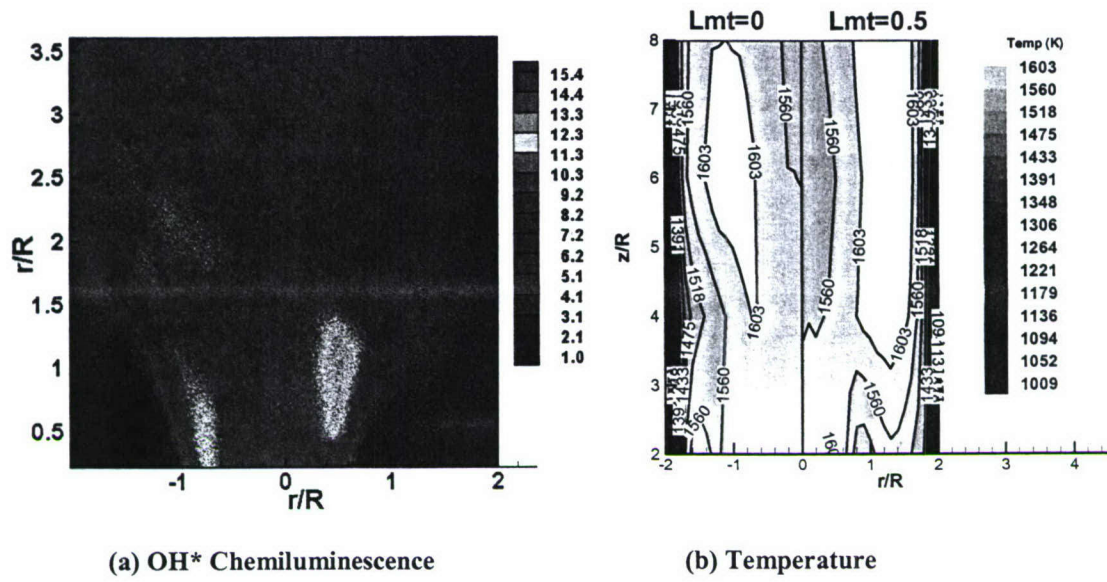
Figure 9: (a) OH* chemiluminescence image for $L_{mt}=0.5$: $\Phi=0.57$, $T_3=230°C$, $m_a=0.032kg/s$, $C_R=1$; (b) comparison of temperature distribution for $L_{mt}=0$ and 0.5: $\Phi=0.5$, $T_3=230°C$, $m_a=0.026kg/s$, $C_R=1$.
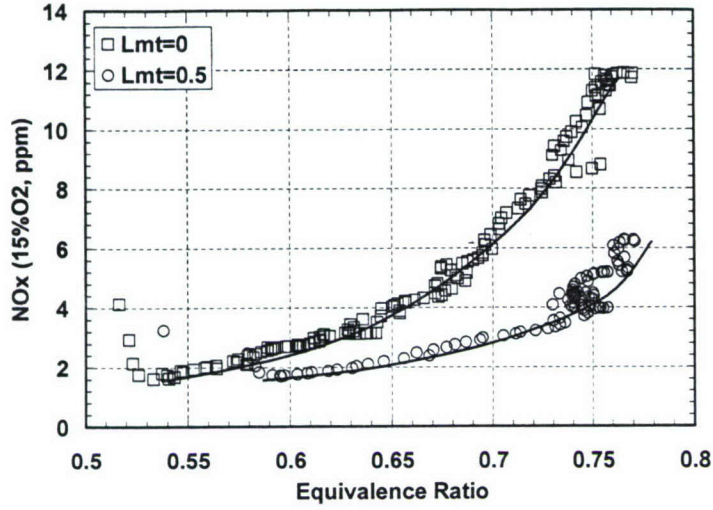
(a)

(b)

Figure 10: Comparison of NO_x and CO for L_{mt}=0 and 0.5: C_R=1, T_3=230°C, m_a=0.032kg/s.
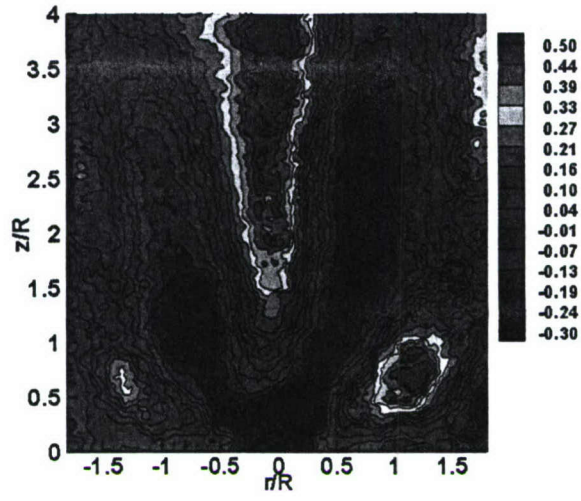
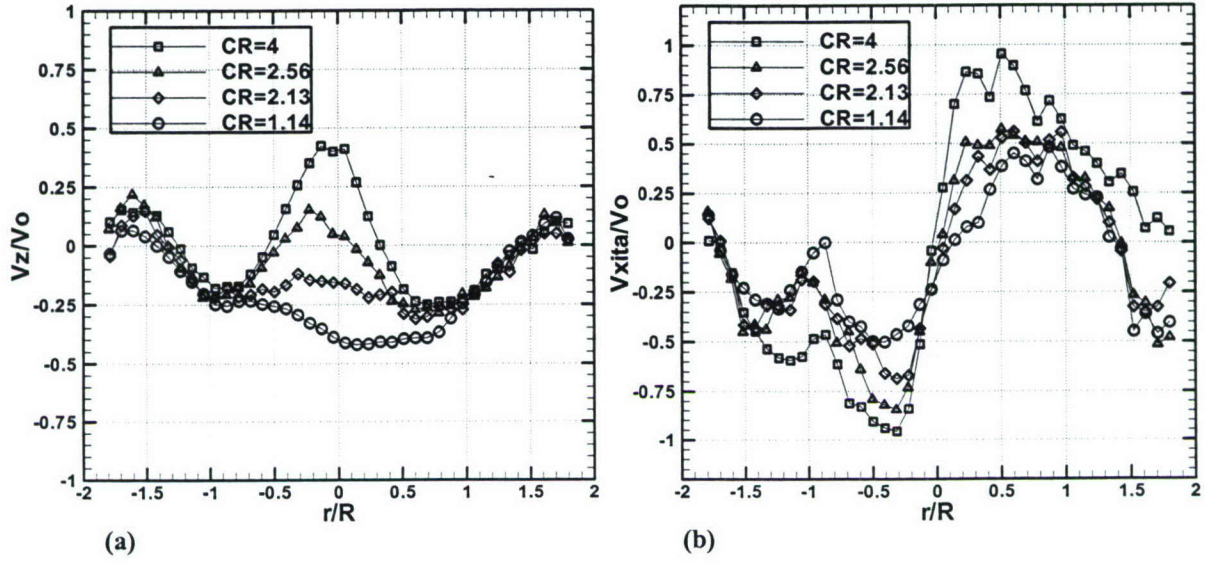**Figure 11: Contours of V_z/V_0 at $C_R= 4$: m_a=0.032kg/s, L_{mt}=0, T_3=23°C.**

Figure 12: Comparison of velocity profiles of (a) V_z/V_0 and (b) V_θ/V_0 for C_R=1.14, 2.13, 2.56, and 4 at z/R=2: m_a=0.032kg/s, L_{ml}=0, T_3=23°C.
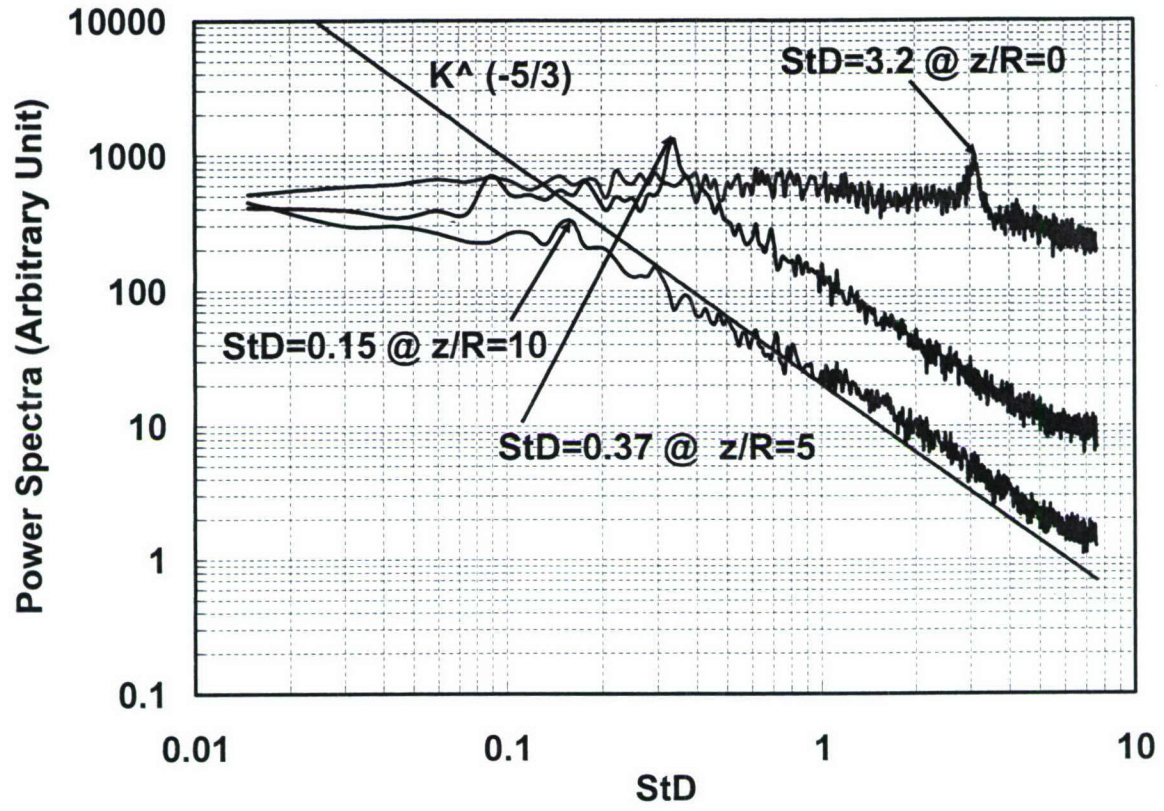
Figure 18: Spectra of velocity of V and W components at locations: r/R=0.4, z/R=0, 5, and 10 for C_R=4: m_a=0.032kg/s, L_{mt}=0, T_3=23°C.
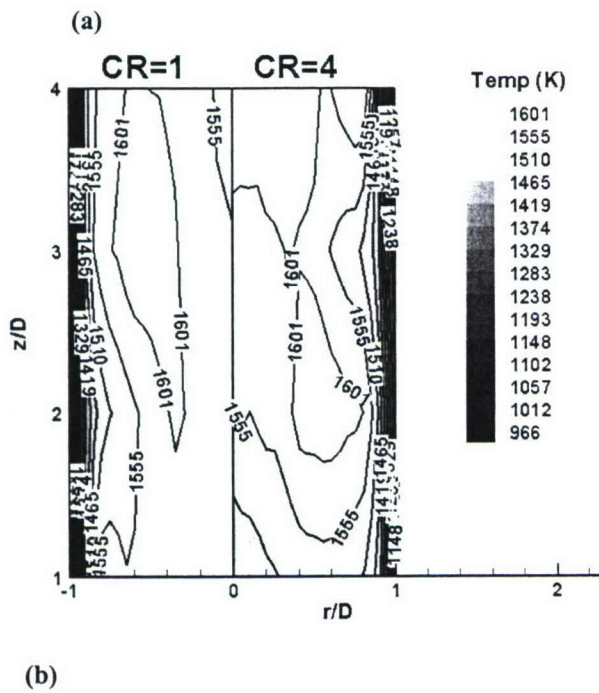
(a)

(b)
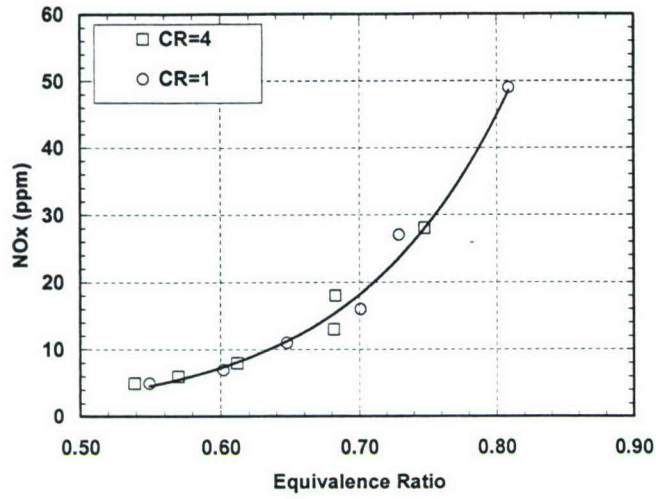
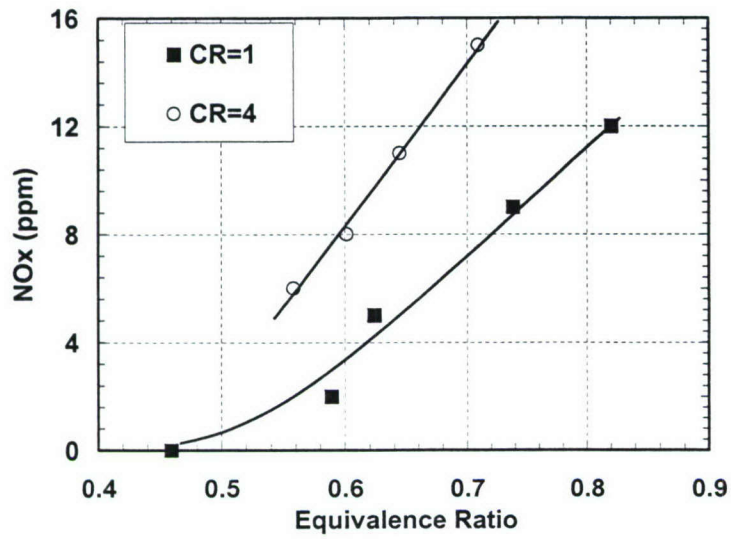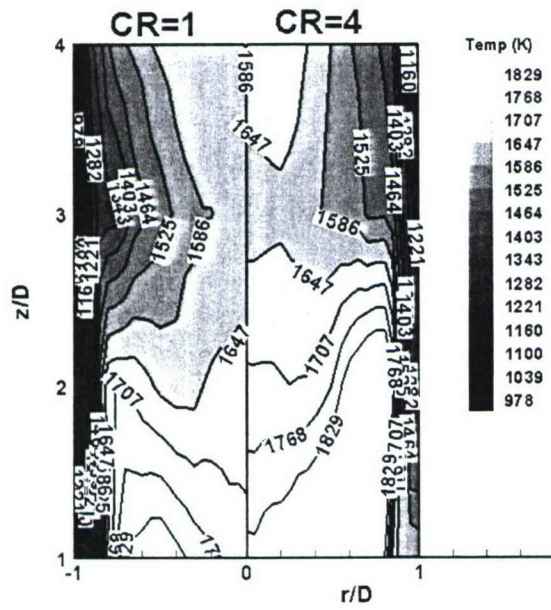Figure 19: Comparison of (a) NO_x emissions; (b) temperature distribution at Φ =0.5 between C_R=1 and 4, gaseous fuel, T_3=230°C, m_a=0.026kg/s.

(a)

(b)

Figure 130: Comparison of (a) NO$_x$ emissions; (b) temperature distribution Φ=0.5 between C_R=1 and 4,

Ethanol, T_3=230°C, m_a=0.032kg/s.

Reference

1. Gupta, A. K., "Gas Turbine Combustion: Prospects and Challenges", *Energy Conversation Management*, Vol.38, No. 10-13, 1997, pp 1311-1318.

2. Doebbling. K., Knopfl, H. P., Polifke, W., Winkler, D., Steinback, C., And Sattelmayer, T., "Low-NOx Premixed Combustion of Mbtu fuels using the ABB Double Cone Burner (EV Burner)", *Transactions of the ASME Journal of Gas Turbines and Power*, V. 118, 1996, pp. 46-53.

3. Snyder, T. S., Rosfjord, T. J., McVey, J. B., Hu, A. S. and Schlein, B. C., "Emission and Performance of a Lean- Premixed Combustion Gas Fuel Injection System for Aeroderative Gas Turbine Engines", *Transactions of the ASME Journal of Gas Turbines and Power*, Vol 118, 1996, pp, 38-45.

4. Docquier, N., Candel, S., "Combustion Control and Sensors: a Review", *Progress in Energy and Combustion Science*, Vol. 28, 2002, pp 107-150.

5. Pandalai, R. P., Mongia, H. C., "Combustion Instability Characteristics of Industrial Engine Dry Low Emission Combustion Systems", AIAA Paper 98-3379, 1998.

6. Gupta, A. K., Ong, L. H., and Marchionna, N., "NOx Reduction and Combustion Phenomena in the Multi-annular Gas Turbine Swirl Burner", AIAA Paper 87-2036, 1987.

7. Hussain, U. S., Andrews, G. E., Cheung, W. G., and Shahabadi, A. R., "Low NO_x Primary Zones Using Jet Mixing Shear Layer Combustion," 1988, ASME 88-GT-308.

8. Terasaki, T., and Hayashi, S., "The Effects of Fuel-air Mixing on NO_x Formation in Non-premixed Swirl Burners," *Twenty-Sixth Symposium (International) on Combustion/The Combustion Institute*, 1996, pp. 2733-2739.

9.   Grinstein, F. F., Young, T. R., Gutmark, E. J., Li, G., Hsiao, G. and Mongia, H., "Flow Dynamics in a Swirl Combustor", Journal of Turbulence, July, 2002.

10. Wang, S., and Young, V., "Modeling of Gas Turbine Swirl Cup Dynamics, Part 5: Large Eddy Simulations of Cold Flow," AIAA-2003-6105, 2003, Reno, NV.

11. Cannon, S. M., and Smith, C. E., "LES Predictions of Combustor Emissions in an Aero Gas Turbine Engine," AIAA-2003-4521, 2003, Huntsville, AL.

12. Shaddix, C. R., "Correcting Thermocouple Measurements for Radiation Loss: a Critical Review", Proceedings of the 33rd National Heat Transfer Conference, 1999, Albuquerque, New Mexico.

13. Schadow, K., and Gutmark, E., "Combustion Instability Related to Vortex Shedding in Dump Combustors and Their Passive Control", *Progress in Energy and Combustion Sciences*, **18**, 117-132, 1992.

14. Chao, Y. C., Leu, J. H. and Hung, Y. F., "Downstream Boundary Effects on the Spectral Characteristics of a Swirling Flow Field", *Experiments in Fluids,* **10**, 1991, pp. 341-348

15. Najm, H. N., Paul, P. H., Mueller C. J., and Wyckoff, P. S., "On the Adequacy of Certain Experimental Observables as Measurements of Flame Burning Rate", Combustion and Flame, Vol. 113, 1998, pp.312-332.

16. Li, G., Gutmark, E. J., "Experimental and Numerical Studies of the Velocity Field of a Triple Annular Swirler", GT-2002-30069, *Proceeding of 2002 International Gas Turbine Institute*, 2002.

17. Li, G., Gutmark, E. J., "Flow field measurement of a Triple Swirler Spray Combustor', AIAA-2002-4010, Joint Propulsion Conference and Exhibit, June, 2002, Indianapolis.

18.   Syred, N. and Beer, J. M., 1974, "Combustion in Swirling Flow: A Review", *Combustion and Flame*, Vol. 23, pp. 143-201.

19.   Escudier, M. P. and Keller, J. J., "Recirculation in Swirling Flow: A Manifestation of Vortex Breakdown", *AIAA Journal*, Vol. 23, NO. 1, 1985, pp.111-116.

20.   Li, G., Gutmark, E., "Effects of Exhaust Nozzle Geometry on Combustor Flow Field and Combustion Characteristics", *Proceeding of 30th Combustion Symposium (International)/The Combustion Institute*, 2004.